Geochemical Perspectives Letters

Ocean mixing timescale through time and implications for the origin of iron formations

C.X. Liu, A. Capirala, S.L. Olson, M.F. Jansen, N. Dauphas

Supplementary Information

The Supplementary Information includes:

- Parameterization of the effect of tidal dissipation and wind energy input on diapycnal mixing
- Modification of day length in cGENIE
- Setup of ExoPlaSim simulations and boundary conditions for cGENIE
- Setup of Nd isotope modelling in cGENIE
- Supplementary Figures S-1 to S-13
- Supplementary Table S-1
- Supplementary Information References

Parameterization of the effect of tidal dissipation and wind energy input on diapycnal mixing

GOLDSTEIN, the ocean circulation model within cGENIE, uses a stratification-dependent diapycnal mixing scheme (Oliver and Edwards, 2008):

$$\kappa(z) = \kappa_c f(z) \times (\rho_{z,lev}(z)/\rho_z(z)), \qquad \text{(Eq. S-1)}$$

where $f(z) = e^{-(2500m-z)/700m}$ is a reference vertical profile exponentially growing with depth and equal to 1 at a depth of 2500 m, $\rho_z(z)$ is the density stratification, $\rho_{z,lev}(z) = (-5.5 \times 10^{-3})e^{z/650m}\ kg\ m^{-4}$ is a reference stratification profile, and κ_c is the diffusivity at 2500 m when $\rho_z(z) = \rho_{z,lev}(z)$. κ_c is treated as an adjustable parameter and is set to $2.5 \times 10^{-5}\ m^2\ s^{-1}$ in our present-day ocean reference case. The resulting diffusivity profile is broadly consistent with observations (Fig. S-1), with values below $10^{-5}\ m^2\ s^{-1}$ in the thermocline and around $10^{-4}\ m^2\ s^{-1}$ at depth (Kunze *et al*., 2006).

For a given stratification, with its effect explicitly accounted for in Eq. S-1, diapycnal diffusivity κ is expected to be proportional to the turbulent kinetic energy dissipation rate ε in the ocean interior, which derives mainly from breaking of internal waves that are ultimately driven by lunisolar tides and surface wind stress (0.3 and 0.1 TW respectively for input rates of energy into vertical mixing below the mixed layer, Yang *et al*., 2017). We therefore expect $\kappa_c/\kappa_{c,m} = \varepsilon/\varepsilon_m = (\varepsilon_t + \varepsilon_w)/\varepsilon_m = (\varepsilon_t/\varepsilon_{t,m})(\varepsilon_{t,m}/\varepsilon_m) + (\varepsilon_w/\varepsilon_{w,m})(\varepsilon_{w,m}/\varepsilon_m)$, where the subscript m indicates present-day conditions, ε_t is the tidal energy dissipation rate, and ε_w is wind-driven turbulent dissipation rate. Waterhouse *et al.* (2014) suggest that tides contribute about 3/4 of the dissipation rate today, thus indicating that $\varepsilon_{t,m}/\varepsilon_m \approx 3/4$, while $\varepsilon_{w,m}/\varepsilon_m \approx 1/4$. We therefore have,

$$\kappa_c/\kappa_{c,m} = \frac{3}{4}(\varepsilon_t/\varepsilon_{t,m}) + \frac{1}{4}(\varepsilon_w/\varepsilon_{w,m}). \quad \text{(Eq. S-2)}$$

Lunisolar tides would have changed in the past due to the greater proximity of the Moon and different continentalities. Assuming a present-day continental configuration, Webb (1982) calculated the influence of Earth-Moon distance on tidal dissipation through time. Assuming that the fraction of tidal dissipation that contributes to deep ocean mixing stayed roughly constant through time, the results suggest that $\varepsilon_t/\varepsilon_{t,m} = 0.7, 0.7, 1.6, 1.9, 2.7$ at 1, 1.6, 2.5, 2.8 and 3.6 Ga respectively.

Davies *et al*. (2020) found that the deep ocean tidal dissipation rate could vary by about a factor of 4 depending on the continental configuration. To take the continentality effect into account, we therefore apply a factor of 0.5 to the minimum $\varepsilon_t/\varepsilon_{t,m}$ and a factor of 2 to the maximum $\varepsilon_t/\varepsilon_{t,m}$ obtained from Webb (1982), resulting in a likely range for $\varepsilon_t/\varepsilon_{t,m}$ between 0.35 and 5.4.

We estimate $\varepsilon_w/\varepsilon_{w,m}$ in our simulations by estimating the spatially integrated wind energy dissipation over the ocean surface and normalizing it with the present-day value,

$$\frac{\varepsilon_w}{\varepsilon_{w,m}} = \frac{p}{p_m}\frac{\int v^2 dA}{\int {v_m}^2 dA}, \quad \text{(Eq. S-3)}$$

where p is mean surface pressure in bar and v is surface wind speed in m/s. We calculate $\varepsilon_w/\varepsilon_{w,m}$ for three groups of sensitivity experiments: continentality, surface pressure, and day length, as well as all the historical simulations from ExoPlaSim. The minimum and maximum $\varepsilon_w/\varepsilon_{w,m}$ values across all simulations are 0.61 and 1.7, which we use as the likely range for our diffusivity sensitivity experiments.

To estimate the minimum and maximum diffusivities, we combine the minimum and maximum of $\varepsilon_t/\varepsilon_{t,m}$ and $\varepsilon_w/\varepsilon_{w,m}$ respectively, which yields $\kappa_{c,min} = 1.0 \times 10^{-5}\, m^2\, s^{-1}$ and $\kappa_{c,max} = 1.1 \times 10^{-4}\, m^2\, s^{-1}$. Including the present-day baseline case with $\kappa_c = 2.5 \times 10^{-4}\, m^2\, s^{-1}$, and an additional intermediate value with $\kappa_c = 6.9 \times 10^{-5}\, m^2\, s^{-1}$ we therefore have four experiments in our diffusivity sensitivity series: $\kappa_c = 1.0 \times 10^{-5}, 2.5 \times 10^{-5}, 6.9 \times 10^{-5}, 1.1 \times 10^{-4}\, m^2 s^{-1}$. For the historical period simulations, we take $\varepsilon_t/\varepsilon_{t,m}$ for the corresponding time period from Webb (1982) and the estimated $\varepsilon_w/\varepsilon_{w,m}$ values from Eq. S-3 specific to the respective simulation. The resulting diapycnal diffusivity values, computed using Eq. S-2, are provided in Table 1.

Modification of day length in cGENIE

Solar day length was explicitly hard-coded at its present-day value (86400 seconds/day) in the GOLDSTEIN ocean, GOLDSTEIN-SEAICE sea-ice, and EMBM atmosphere modules within the cGENIE model. In addition, present-day sidereal day length was implicitly used in deriving the scaled Coriolis coefficient $fsc = 2 \times 7.2921 \times 10^{-5} = 2 \times 2\pi/86164$. To enable simulations with day lengths (rotation rates) different from Earth's modern 24 hr day length, we introduce solar day length and sidereal day length in cGENIE as namelist parameters, following the instructions in Ridgwell (2017). The code for the version of the "muffin" release of the cGENIE Earth system model used in this paper is tagged as v0.9.50 and is assigned a DOI: 10.5281/zenodo.10798347.

cGENIE assumes a default year length of 365.25 days/year. In this paper, we modify the number of days per year such that all simulations have the same orbital period (total seconds/year).

Setup of ExoPlaSim simulations and boundary conditions for cGENIE

Atmospheric modeling in ExoPlaSim. cGENIE does not model a dynamic atmosphere and requires prescribed atmospheric and surface boundary conditions to force ocean circulation. These inputs are in the form of wind stress fields and zonally-averaged planetary albedo. The variations in wind patterns and planetary albedo are significant when varying rotation rate and surface pressure, so to account for the effect on wind-driven circulation, we first conduct equivalent simulations using ExoPlaSim v. 3.0.6 (Paradise *et al*., 2022; pypi.org/project/exoplasim/3.0.6/), a modified version of the Planet Simulator (PlaSim, Fraedrich *et al*., 2005). ExoPlaSim is a fast atmospheric GCM modified to

simulate a wider variety of non-Earth-like planets, including different rotation rates and surface pressures. We run our simulations at T21 resolution (32 latitudes by 64 longitudes), 10 atmospheric layers, and all present-day Earth-like parameters except for rotation rate, surface pressure, and land map as varied across our experiments. ExoPlaSim uses a slab ocean that lacks dynamic heat transport and simulates a mixed layer of constant depth (set in our experiments to 100 m) and constant heat capacity (set by the model to 4180 J kg^{-1} K^{-1}). A present-day Earth-like climate is also imposed for all experiments at 1 atm pressure by using modern solar flux and pre-industrial levels of pCO_2, and climate is thus only allowed to vary in response to our parameters of interest. ExoPlaSim's atmospheric composition comprises only N_2, CO_2, H_2O, and O_3, which is sufficient to produce a realistic behavior. At pressures other than 1 atm, pN_2 and pCO_2 are both multiplied to keep their relative amounts constant.

Ozone is handled differently in our experimental configurations. Due to its role in stratospheric warming, O_3 is necessary to produce modern Earth surface temperatures and reasonable extents of sea-ice in the model. However, the climate responds unrealistically to ozone present in the atmosphere at higher surface pressures. When pressures increase, a higher number of collisional interactions between molecules in the atmosphere affects the absorption and emission of infrared radiation, causing increased greenhouse warming (termed pressure broadening). This effect is parameterized in ExoPlaSim as an idealized multiplicative parameter that alters absorption by O_3, CO_2, and H_2O by adjusting the amount of effective absorber (Paradise *et al.*, 2021). Pressure broadening offsets the significant cooling effect of Rayleigh scattering that also occurs at higher pressures. At 2 atm surface pressure, we find that O_3 generates a strong warming positive feedback with water vapor when pressure broadening is applied to both absorbers, generating surface temperatures that are unrealistic for any time period in our study (mean global temperatures upwards of 60 ° C and maximum temperatures around 75-80 °C). Therefore, we enable O_3 only in simulations where the surface pressure is 1 atm. A 1 atm simulation without ozone is provided for comparison with the pressure sensitivity experiments (Fig. S-2).

Boundary conditions in cGENIE. To derive required boundary conditions for cGENIE's ocean circulation (wind fields and planetary albedo), we implement modifications to the 'muffingen' open source software version v0.9.21 (DOI: 10.5281/zenodo.10802839), which in its original state takes output files from coupled GCM experiments to create a full set of input files for running an equivalent simulation in cGENIE. Our modified scripts re-grid and convert only ExoPlaSim wind stress, velocity, and radiation outputs to input files for cGENIE's 36×36 grid. A supplementary script

converts cGENIE land-sea mask files to ExoPlaSim landmap files so that the spatial boundary conditions correctly align with the topography of the cGENIE experiment.

Wind stress fields required by cGENIE's GOLDSTEIN, GOLDSTEIN-SEAICE, and EMBM modules are in the form of x- and y- component (eastward and northward) wind stress at the u and v grid points of cGENIE's Arakawa C grid. An additional wind speed field, computed as the vector magnitude of the x- and y- wind velocity from ExoPlaSim, is used by the EMBM. Planetary albedo is calculated as the ratio between total annual incoming and outgoing shortwave radiation at the top of the atmosphere and it is regridded to a zonally averaged planetary albedo. All regridded products are generated from an average of the last 10 simulation years in ExoPlaSim to account for minor inter-annual variations in output variables or different monthly averaging at non-present-day day lengths. Finally, we adjust the wind-stress scaling parameter in the cGENIE model to achieve comparable modern global ventilation ages using ExoPlaSim wind fields. Because cGENIE by default calibrates its wind-driven circulation to the magnitude of its own internal wind field when external GCM wind fields are not applied, this adjustment is necessary to compensate for the differences in how the two models—ExoPlaSim and cGENIE—calculate and report the average magnitude of wind stress (*e.g.*, Crichton *et al.*, 2021).

Setup of Nd isotope modelling in cGENIE

To estimate the Nd-$\boldsymbol{\varepsilon}_{\mathrm{Nd}}$ budget for Archean oceans (Table S-1), we need to know the following:

1. The residence time of Nd.
2. Nd input fluxes (g/yr) of rivers ($\phi_{\mathrm{Nd,r}}$), aeolian dust ($\phi_{\mathrm{Nd,d}}$), hydrothermal fluids ($\phi_{\mathrm{Nd,h}}$) and benthic sediments ($\phi_{\mathrm{Nd,s}}$).
3. Global mean Nd isotopic compositions of seawater ($\varepsilon_{\mathrm{Nd,sw}}$), river ($\varepsilon_{\mathrm{Nd,r}}$), aeolian dust ($\varepsilon_{\mathrm{Nd,d}}$), hydrothermal fluid ($\varepsilon_{\mathrm{Nd,h}}$), and benthic sediment ($\varepsilon_{\mathrm{Nd,s}}$) sources.

We estimate $\phi_{\mathrm{Nd,r}}$, $\phi_{\mathrm{Nd,d}}$, and $\phi_{\mathrm{Nd,h}}$ following the approach used by Dauphas *et al.* (2024) for iron. We assume that at steady-state, the Nd flux from rivers scales with the rate of continental chemical weathering, which itself is going to scale with the rate of CO_2 degassing through

$$\phi_{\mathrm{Nd,r}}(t) = r_{CO_2} r_{\phi_{\mathrm{mantle}}} \phi_{\mathrm{Nd,r}}(0), \qquad \text{(Eq. S-4)}$$

where $r_{CO_2} = 0.8$ is the Archean to present-day ratio of the fraction of CO_2 drawdown associated with continental weathering (Krissansen-Totton *et al.*, 2018), $r_{\phi_{\text{mantle}}} = 2.3$ is the Archean to present-day ratio of mantle heat flux (Patočka *et al.*, 2020), and $\phi_{\text{Nd,r}}(0) = 1.5 \times 10^9$ g/yr is the present-day global Nd river input flux (Xu *et al.*, 2023), resulting in $\phi_{\text{Nd,r}}(t) = 2.76 \times 10^9$ g/yr into the Archean oceans. The Nd river flux may have been affected by its speciation and pH-dependent adsorption on solid particles (Goldstein and Jacobsen, 1987), which is not accounted for here due to lack of constraints. The Archean to present-day ratio of mantle heat flux is also uncertain, as it could have been significantly lower than what we adopted here. Indeed, Korenaga (2008) argued that the mantle heat flux did not change much since 4 Ga.

For the flux of dust, we use the following scaling,

$$\phi_{\text{Nd,d}}(t) = r_A \cdot \phi_{\text{dust}}(0) \cdot r_{[Nd]_{EC}} \cdot [Nd]_d(0) \cdot f(t), \quad \text{(Eq. S-5)}$$

where $r_A = 0.5$ is the Archean to present-day ratio of areal extent of emerged continents (Korenaga *et al.*, 2017), $\phi_{\text{dust}}(0) = 440\ Tg/yr$ is the present-day dust input flux (Wu *et al.*, 2020), $r_{[Nd]_{EC}} = 0.65$ is the Archean to present-day ratio of Nd concentration of emerged continents (Ptáček *et al.*, 2020), $[Nd]_d(0) = 20\ \mu g/g$ is the present-day global mean Nd concentration in dust (Goldstein *et al.*, 1984), and $f(t) = 0.1$ is the Archean fraction of Nd in dust that dissolves along with Fe in seawater (Dauphas *et al.*, 2024; Greaves *et al.*, 1994), resulting in $\phi_{\text{Nd,d}}(t) = 2.86 \times 10^8$ g/yr during the Archean.

In the modern ocean, hydrothermal fluids represent a negligible source and in fact represent a net sink due to scavenging of Nd by particulate iron (German *et al.*, 1990). In the anoxic Archean ocean, high-temperature hydrothermal fluids could have released Fe and Nd into seawater without elemental fractionation (Jacobsen and Pimentel-Klose, 1988). We therefore use the following scaling,

$$\phi_{\text{Nd,h}}(t) = r_{\phi_{\text{hydro}}} \cdot \phi_{\text{hw}}(0) \cdot [Fe]_h(0) \cdot \left(\frac{Nd}{Fe}\right)_{\text{mafic}}(t), \quad \text{(Eq. S-6)}$$

where $r_{\phi_{\text{hydro}}} = 5$ is the maximum Archean to present-day ratio of hydrothermal heat flux (Lowell and Keller, 2003), $\phi_{\text{hw}}(0) = 5.9 \times 10^{16}$ g/yr is the present-day high-temperature hydrothermal water flux (Dauphas *et al.*, 2024), $[Fe]_h(0) = 5.8\ mmol/kg$ is the present-day Fe concentration in high-temperature hydrothermal fluid (Dauphas *et al.*,

2024), and $(Nd/Fe)_{\text{mafic}}(t) = 0.00013$ is the Nd/Fe ratio in Archean mafic rocks (Ptáček *et al.*, 2020), resulting in $\phi_{\text{Nd,h}}(t) = 1.25 \times 10^{10}$ g/yr during the Archean.

In the modern ocean, the flux from benthic sediments accounts for ~95% of total Nd sources (Rempfer *et al.*, 2011; Abbott *et al.*, 2015a, b; Haley *et al.*, 2017; Du *et al.*, 2020). The mechanisms of this benthic sediment Nd input are not yet defined, but the Nd flux seems to be dominated by deep-sea sediments (water depth > 3 km) and may be controlled by the extent of benthic seafloor area and sediment provenance, with no clear influence of the redox state of the sediments (Du *et al.*, 2018). We posit that in the Archean, the sediment source consistently scaled with the flux of other sources (Table S-1).

We make two different assumptions for that scaling: it could either represent 95% of the total flux including hydrothermal, or 95% of the total flux excluding hydrothermal. While the sediment source dominates the overall Nd flux, other sources play significant roles in the Nd cycle as they can influence the ε_{Nd} value of nearby water masses. Assuming that the benthic flux represents 95% of the total, we have $\phi_{\text{Nd}} = (\phi_{\text{Nd,r}} + \phi_{\text{Nd,d}} + \phi_{\text{Nd,h}})/5\% = 3.11 \times 10^{11}$ g/yr and $\phi_{\text{Nd,s}} = 95\%\phi_{\text{Nd}} = 2.95 \times 10^{11}$ g/yr. Assuming that the benthic flux represents 95% of the total excluding hydrothermal, we have $\phi_{\text{Nd,s}} = 5.79 \times 10^{10}$ g/yr and $\phi_{\text{Nd}} = \phi_{\text{Nd,r}} + \phi_{\text{Nd,d}} + \phi_{\text{Nd,h}} + \phi_{\text{Nd,s}} = 7.34 \times 10^{10}$ g/yr. In both cases, the benthic flux dominates all other fluxes (79% to 95% of the total).

For the first assumption, we use $[Nd]_{\text{sw}} = 1.43 \times 10^{-7}$ g/kg by taking the average of the Nd concentrations of 3.1-3.4 Ga seawater estimated from BIF magnetite of Badampahar greenstone belt (Ghosh and Baidya, 2017) and dolomite of Pilbara Block (Yamamoto *et al.*, 2004). For a 1.4×10^{21} kg ocean, this gives a total Nd inventory equal to 2.0×10^{14} g. The calculated Nd residence time in the Archean oceans is therefore $\tau_{\text{Nd}} = Nd/\phi_{\text{Nd}} = (2.0 \times 10^{14}\text{ g})/(3.11 \times 10^{11}\text{ g/yr}) = 643\ yr$. The Nd concentration in the Archean ocean is, however, poorly constrained, and we adopt a constant residence time of 643 yr in all simulations. Therefore, $[Nd]_{\text{sw}}$ becomes 3.37×10^{-8} g/kg for the second assumption.

In the modern ocean, Nd is removed from the water column by scavenging on particles following a first-order kinetic rate law $\phi_{\text{Nd,sink}} = k \cdot dt \cdot [Nd]_{sw}$, where $k = 1/\tau_{\text{Nd}}$ (Bacon and Anderson, 1982; Du *et al.*, 2020). We assume

that Nd removal in Precambrian oceans took place through the same mechanism with the same first-order kinetic law applying, and we set $k = 1/643\ yr^{-1}$ in our model to balance the input fluxes.

We estimate Archean $\varepsilon_{Nd,sw}$, $\varepsilon_{Nd,h}$, $\varepsilon_{Nd,r}$ and $\varepsilon_{Nd,d}$ values by taking the average ε_{Nd} of Superior-type BIFs compiled (Pongola BIF, Alexander *et al*., 2008; Marra Mamba BIF, Alibert and McCulloch, 1993; Benchmark BIF, Frei *et al*., 2008; Central Slave Cover Group BIF, Haugaard *et al*., 2016), depleted mantle-derived rocks (Vervoort and Blichert-Toft, 1999), and detrital sedimentary rocks (Garçon, 2021) respectively, assuming $\varepsilon_{Nd,r} = \varepsilon_{Nd,d}$ as river and dust Nd both reflect continental ε_{Nd}. Taking the average of ε_{Nd} of each rock type during the Archean (Fig. 3a), we have $\varepsilon_{Nd,sw} = +0.63$, $\varepsilon_{Nd,h} = +2.6$, and $\varepsilon_{Nd,r} = \varepsilon_{Nd,d} = -0.42$. We then solve for the benthic sediment isotopic composition $\varepsilon_{Nd,s}$ through a simple mass balance calculation that ensures that the source ε_{Nd} value is equal to seawater (the sink ε_{Nd} value is that of seawater),

$$\varepsilon_{Nd,sw} = \left(\varepsilon_{Nd,r} \times \phi_{Nd,r} + \varepsilon_{Nd,d} \times \phi_{Nd,d} + \varepsilon_{Nd,h} \times \phi_{Nd,h} + \varepsilon_{Nd,s} \times \phi_{Nd,s}\right)/\left(\phi_{Nd,r} + \phi_{Nd,d} + \phi_{Nd,h} + \phi_{Nd,s}\right). \quad \text{(Eq. S-7)}$$

By plugging in the values for Nd fluxes and isotopic compositions from above, we get $\varepsilon_{Nd,s} = +0.56$ for Scenario 1 and $\varepsilon_{Nd,s} = +0.26$ for Scenario 2.

We additionally consider a heterogeneous scenario (Scenario 3) where $\varepsilon_{Nd,s} = \varepsilon_{Nd,h}$ in sediments located closer to the hydrothermal source, and $\varepsilon_{Nd,s} = \varepsilon_{Nd,r}$ in sediments located closer to the continental sources. The magnitude of sediment flux carrying either isotopic signature is proportional to the magnitude of the corresponding flux.

Finally in Scenario 4, to account for the possible heterogeneity in ε_{Nd} values due to coexistence of juvenile and older crust in the late Archean, as is observed in detrital sediments of Archean age (Fig. 3a), we take the ε_{Nd} values of depleted mantle ($\varepsilon_{Nd,c,juv} = +3.4$) and continuous continental crust growth ($\varepsilon_{Nd,c,old} = -3.1$) models at ~2.5 to 3.0 Ga from Garçon (2021) as endmembers for rivers, aeolian dust, and benthic sediments $\varepsilon_{Nd,r}$, $\varepsilon_{Nd,d}$ and $\varepsilon_{Nd,s}$. Detrital sedimentary rocks indicate that this period saw an impulse of juvenile crust production from the depleted mantle (Garçon, 2021). We then solve for the relative contributions of these two endmember ε_{Nd} values into the Archean ocean such that the bulk $\varepsilon_{Nd,sw}$ is reproduced,

$$\varepsilon_{Nd,sw} = \frac{\left[\varepsilon_{Nd,c,old} \times x + \varepsilon_{Nd,c,juv} \times (1-x)\right]\left(\phi_{Nd,r} + \phi_{Nd,d} + \phi_{Nd,s}\right) + \varepsilon_{Nd,h} \times \phi_{Nd,h}}{\phi_{Nd,r} + \phi_{Nd,d} + \phi_{Nd,h} + \phi_{Nd,s}}, \quad \text{(Eq. S-8)}$$

yielding $x = 0.49$, meaning that meaning that 49% of the river, aeolian, and benthic sediment sources have enriched $\varepsilon_{Nd} = -3.1$ and the remaining 51% have depleted $\varepsilon_{Nd} = +3.4$. Such proportion of juvenile crust needed to explain the average BIF ε_{Nd} value is close to the value calculated by Garçon (2021) for the source of detrital sediments during this period (~50%).

The Nd riverine flux is applied in coastal grid cells around the supercontinents in the surface ocean, and the Nd dust flux is applied in all surface ocean grid cells. The Nd hydrothermal flux is applied along 'mid-ocean ridges' between 115°W and 125°W in the bottom ocean, and the Nd sediment flux is applied in all bottom ocean grid cells except those occupied by the hydrothermal flux. Nd sources are balanced by one sink, scavenging, which is parameterized following the first-order rate law discussed above, applied uniformly to all ocean cells.

To test our model's ability to reconstruct the source heterogeneity of ε_{Nd} as observed in the modern ocean and evaluate how sensitive it is to the sediment flux, we model ε_{Nd} in the modern ocean with and without a sediment flux (Fig. S-3). In the simulation aimed at reproducing the modern Nd cycle, we use modern river, dust and sediment Nd input fluxes and corresponding ε_{Nd} values that vary among basins based on Table 1 from Du *et al*. (2020). In the simulation aimed at evaluating the influence of the sediment flux, the global seawater ε_{Nd} is affected only by the river and dust fluxes. Despite variations in ε_{Nd} in the North Atlantic that contrast with observations due to reduced North Atlantic Deep Water formation in our modelled present-day ocean (Fig. S-4), incorporating a sediment Nd source with variable ε_{Nd} significantly improves the model's ability to capture the observed ε_{Nd} heterogeneity between Pacific and Atlantic Oceans, especially at depths >200 m, which is the bathymetry relevant for Precambrian BIF formation (Trendall, 2002).

Supplementary Figures

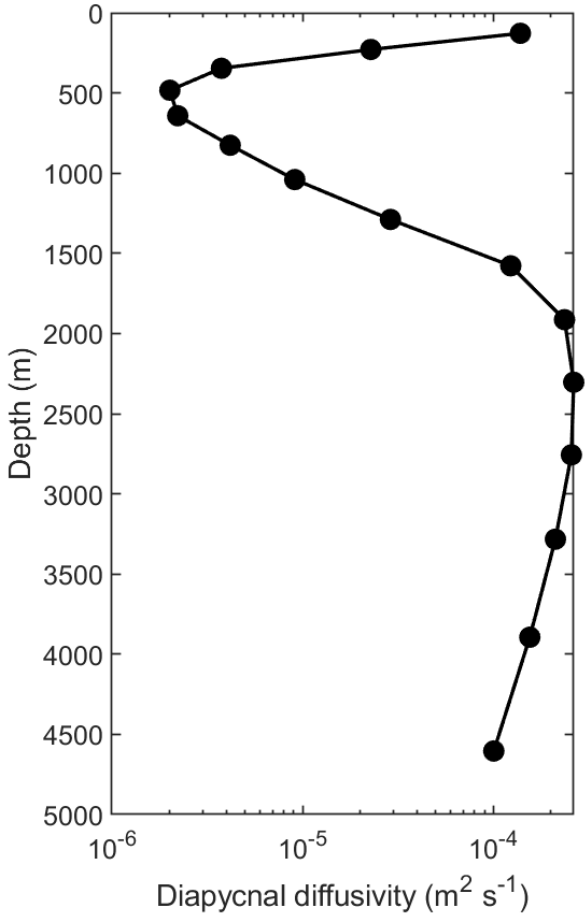

Figure S-1 Depth profile of diapycnal diffusivity in the present-day baseline model simulation. The profile shows the stratification-weighted horizontal average of the model's 3-dimensional diffusivity field.

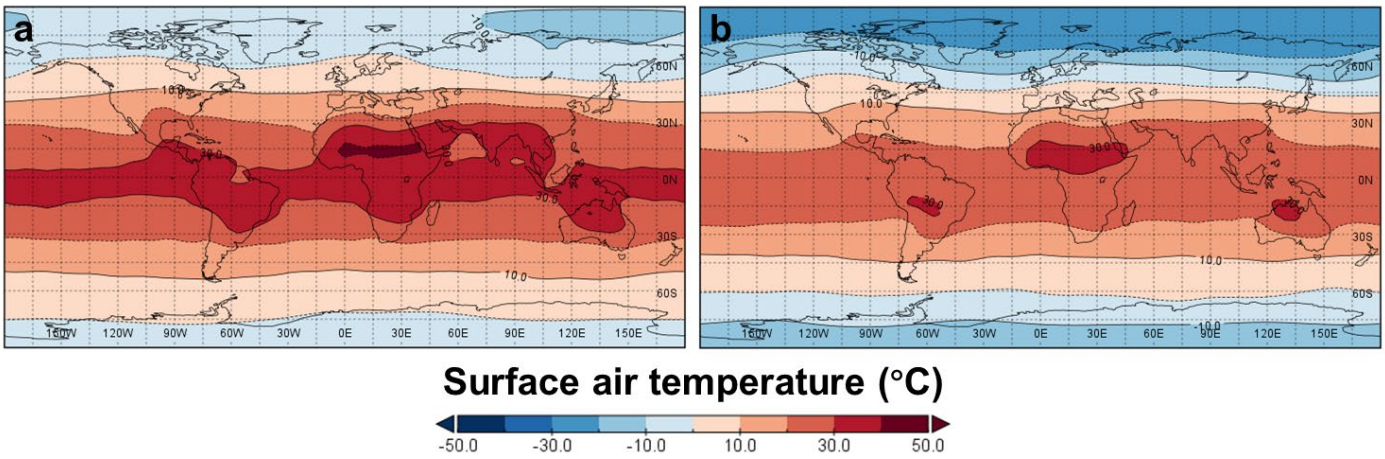

Figure S-2 Annual mean surface air temperature in (a) present-day baseline with ozone and (b) ozone-less baseline.

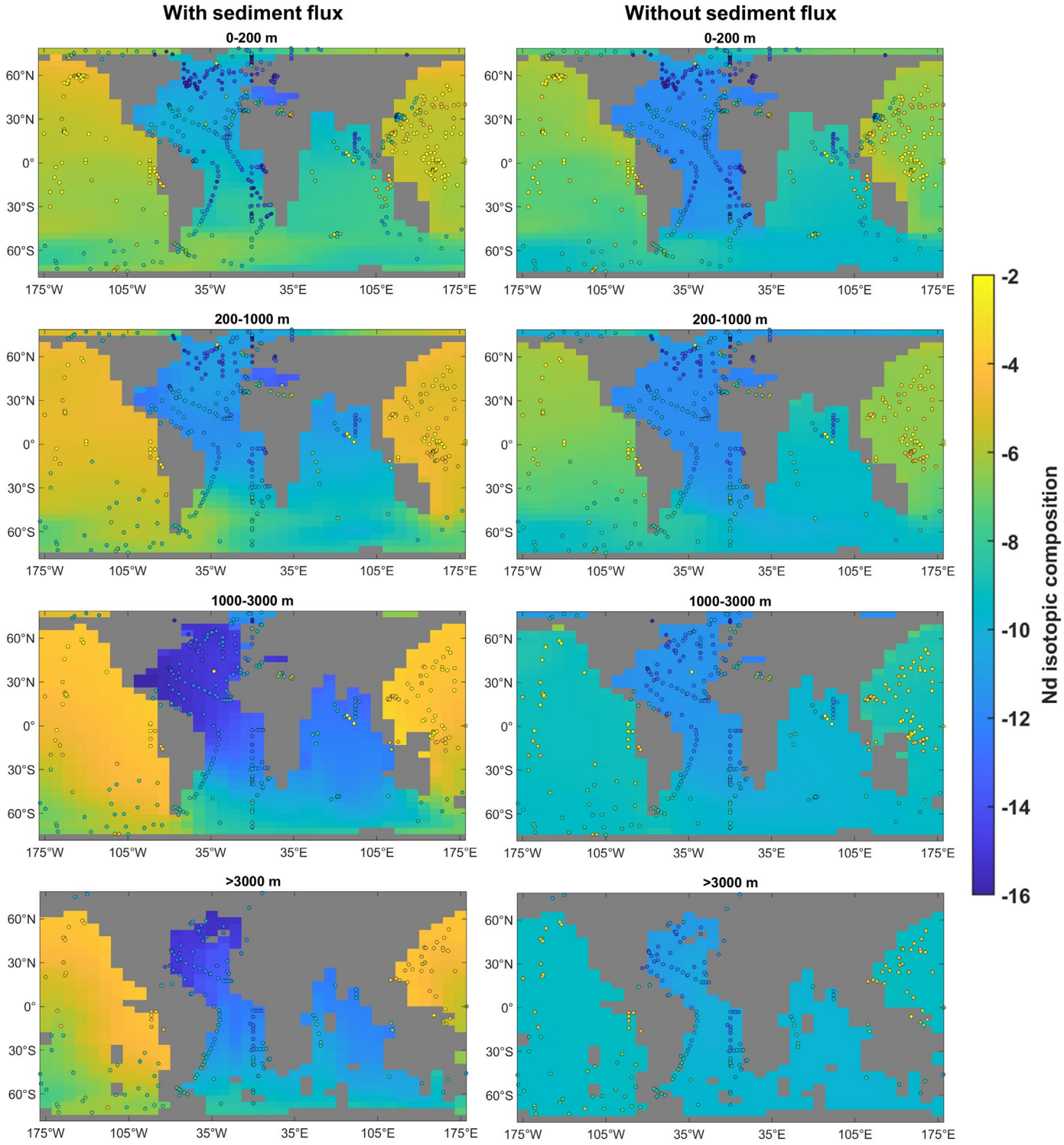

Figure S-3 Modelled Nd isotopic composition in present-day baseline with (left) or without (right) a benthic sediment source. Circles are observational data compiled by Robinson *et al.* (2023).

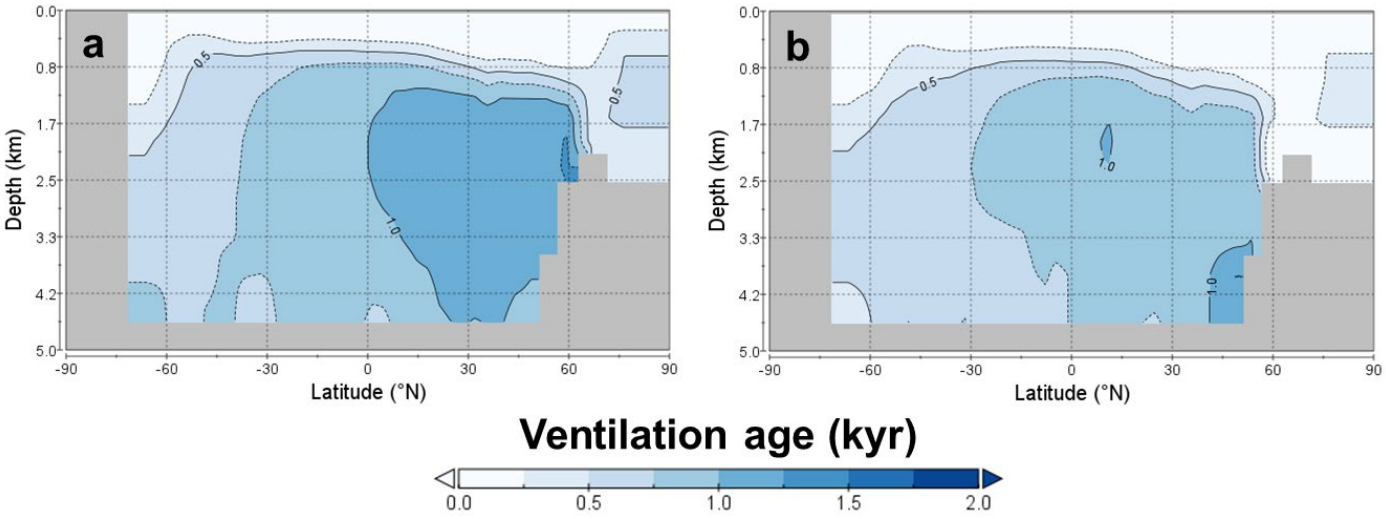

Figure S-4 Zonal mean water mass ventilation age in **(a)** present-day baseline with ozone and **(b)** ozone-less baseline.

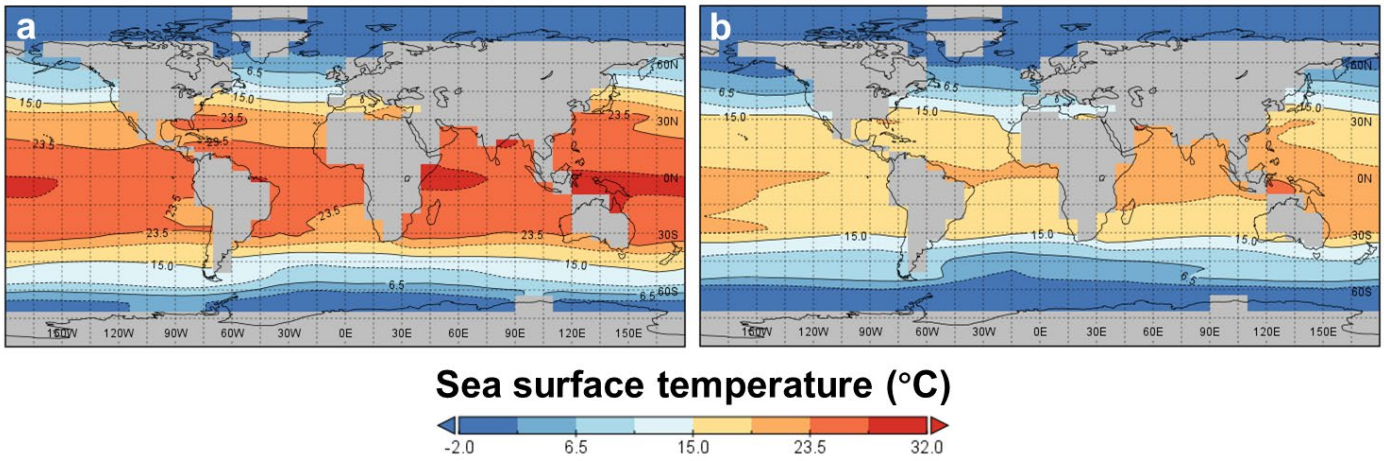

Figure S-5 Annual mean sea surface temperature in **(a)** present-day baseline with ozone and **(b)** ozone-less baseline.

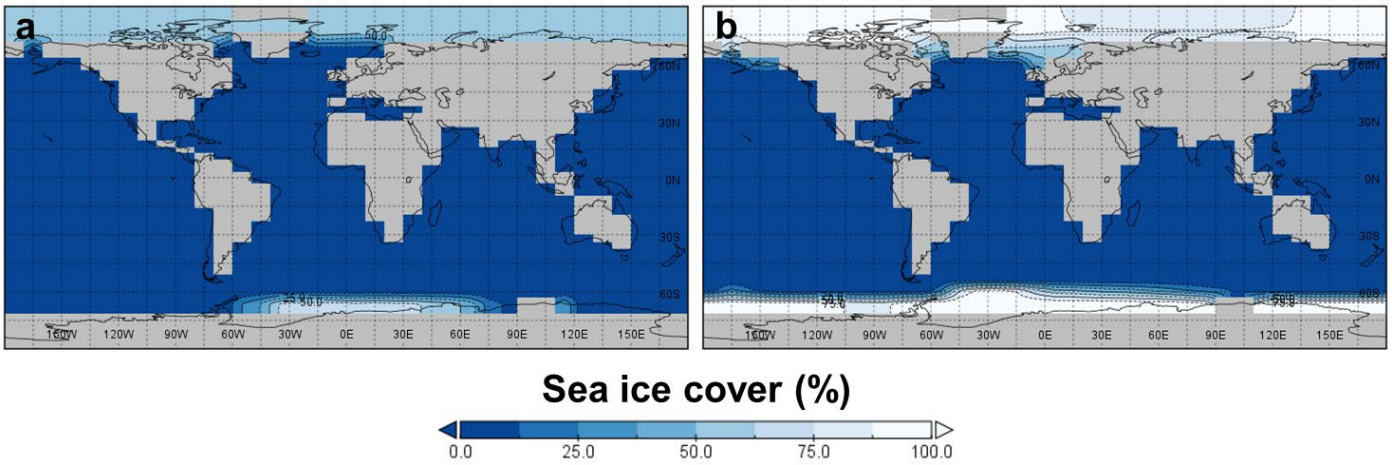

Figure S-6 Annual mean sea ice cover in **(a)** present-day baseline with ozone and **(b)** ozone-less baseline.

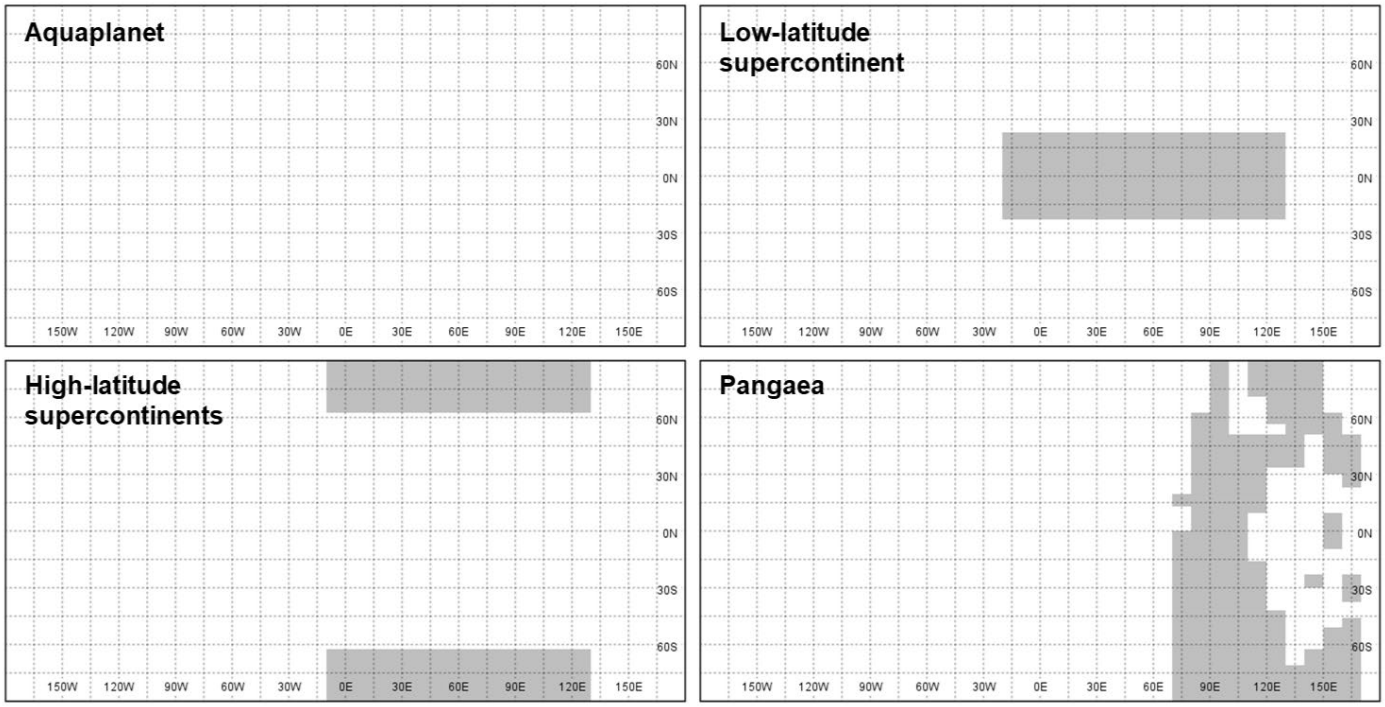

Figure S-7 Continental configurations used in sensitivity and historical simulations.

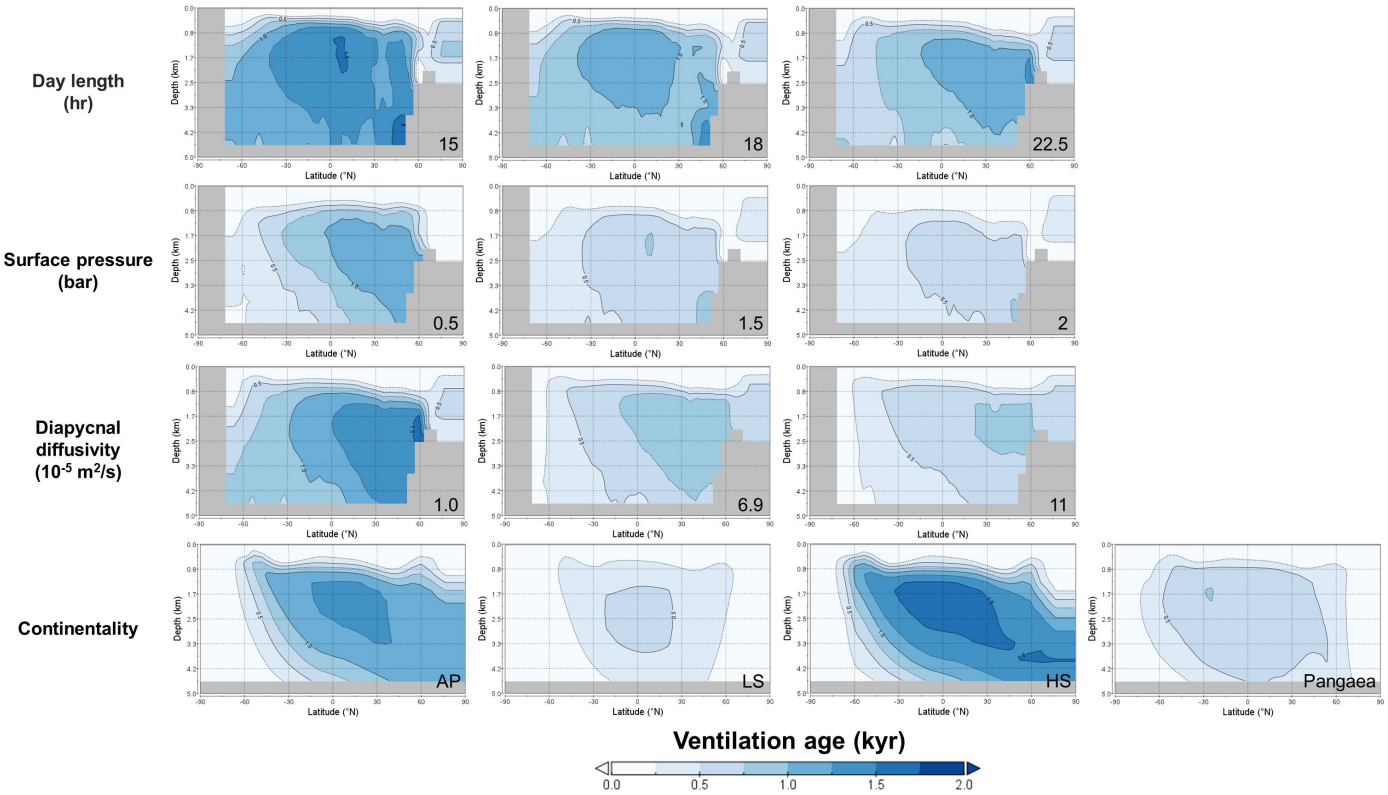

Figure S-8 Zonal mean water mass ventilation age in sensitivity tests. AP: aquaplanet; LS: low-latitude supercontinent; HS: high-latitude supercontinents.

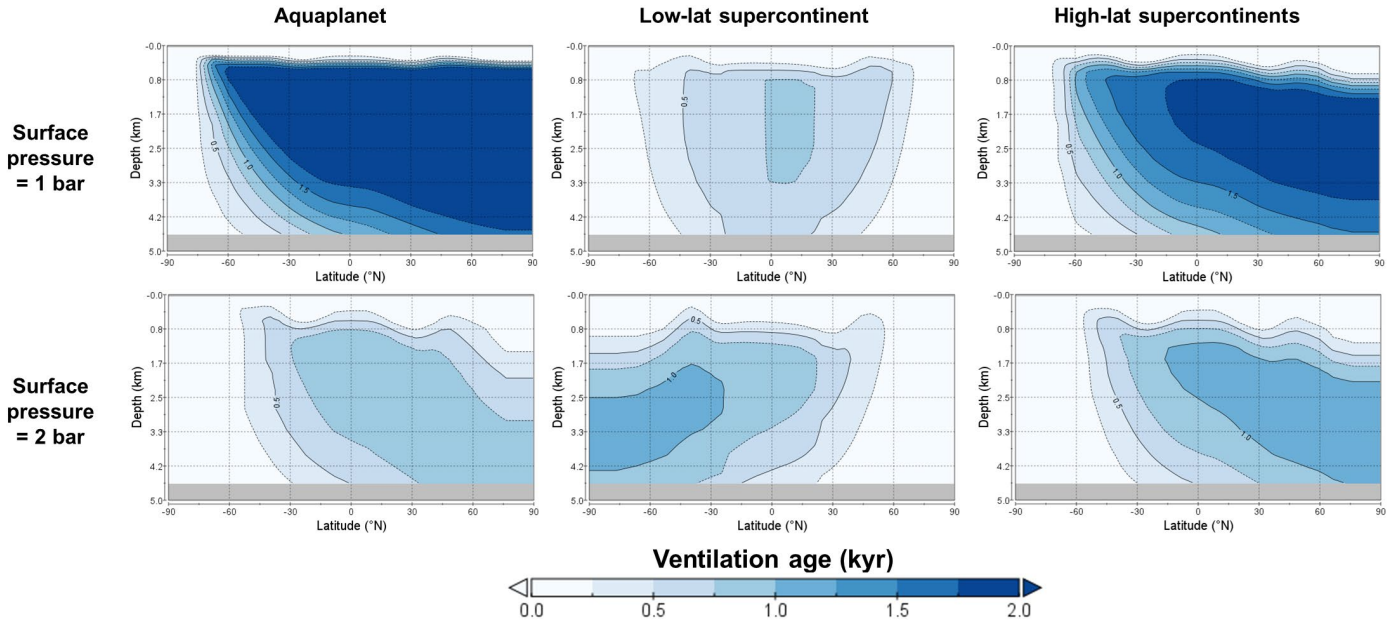

Figure S-9 Zonal mean water mass ventilation age in 'Paleoarchean' simulations with day length = 15 hr and individual diapycnal diffusivities (see Table 1 for details). Note that the color bar is saturated in the top left panel, where the maximum age is 2.4 kyr.

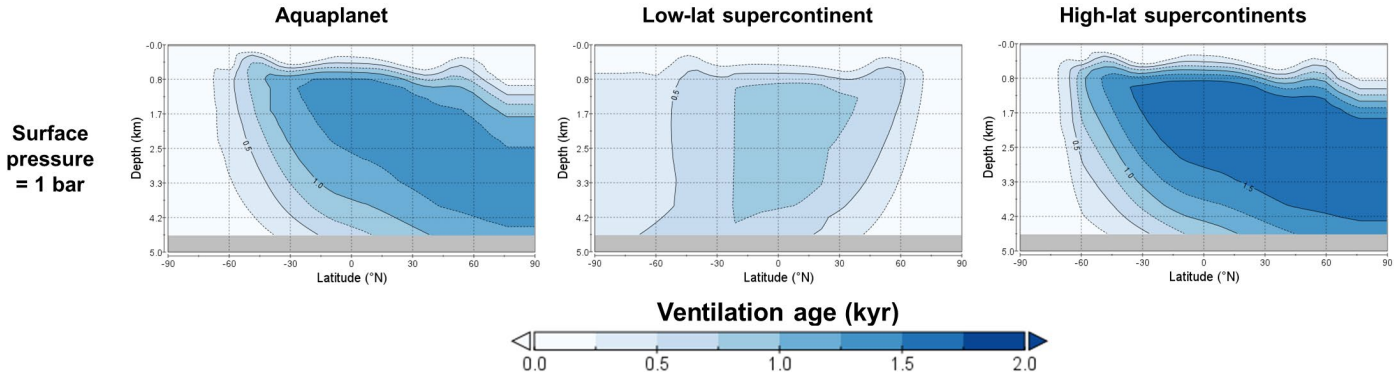

Figure S-10 Zonal mean water mass ventilation age in 'Neoarchean' simulations with day length = 18 hr and individual diapycnal diffusivities (see Table 1 for details).

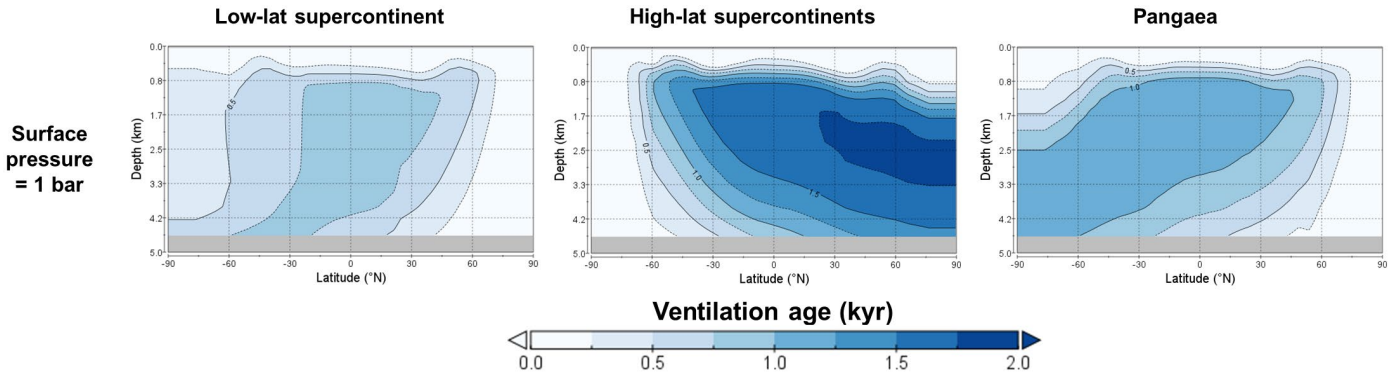

Figure S-11 Zonal mean water mass ventilation age in 'Paleoproterozoic' simulations with day length = 18 hr and individual diapycnal diffusivities (see Table 1 for details).

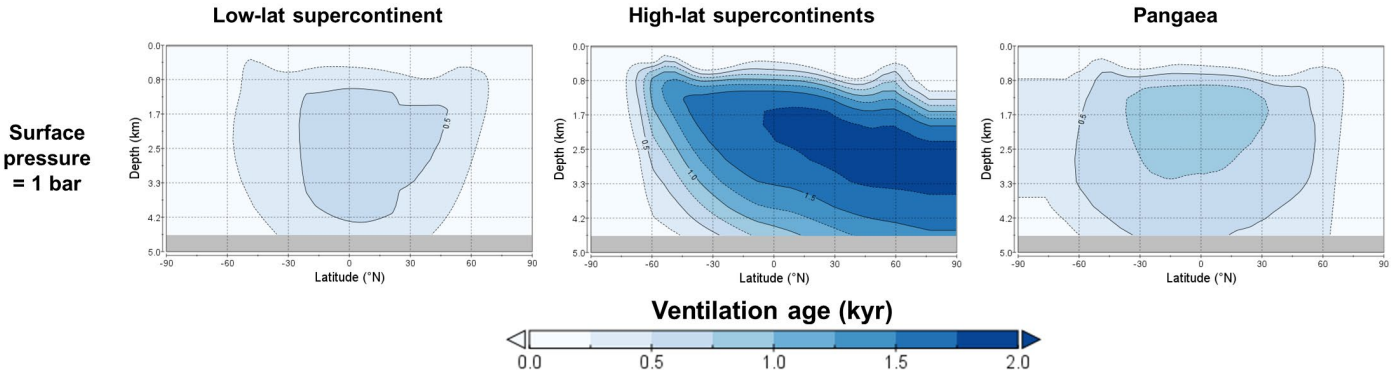

Figure S-12 Zonal mean water mass ventilation age in 'Meso/Neoproterozoic' simulations with day length = 22.5 hr and individual diapycnal diffusivities (see Table 1 for details).

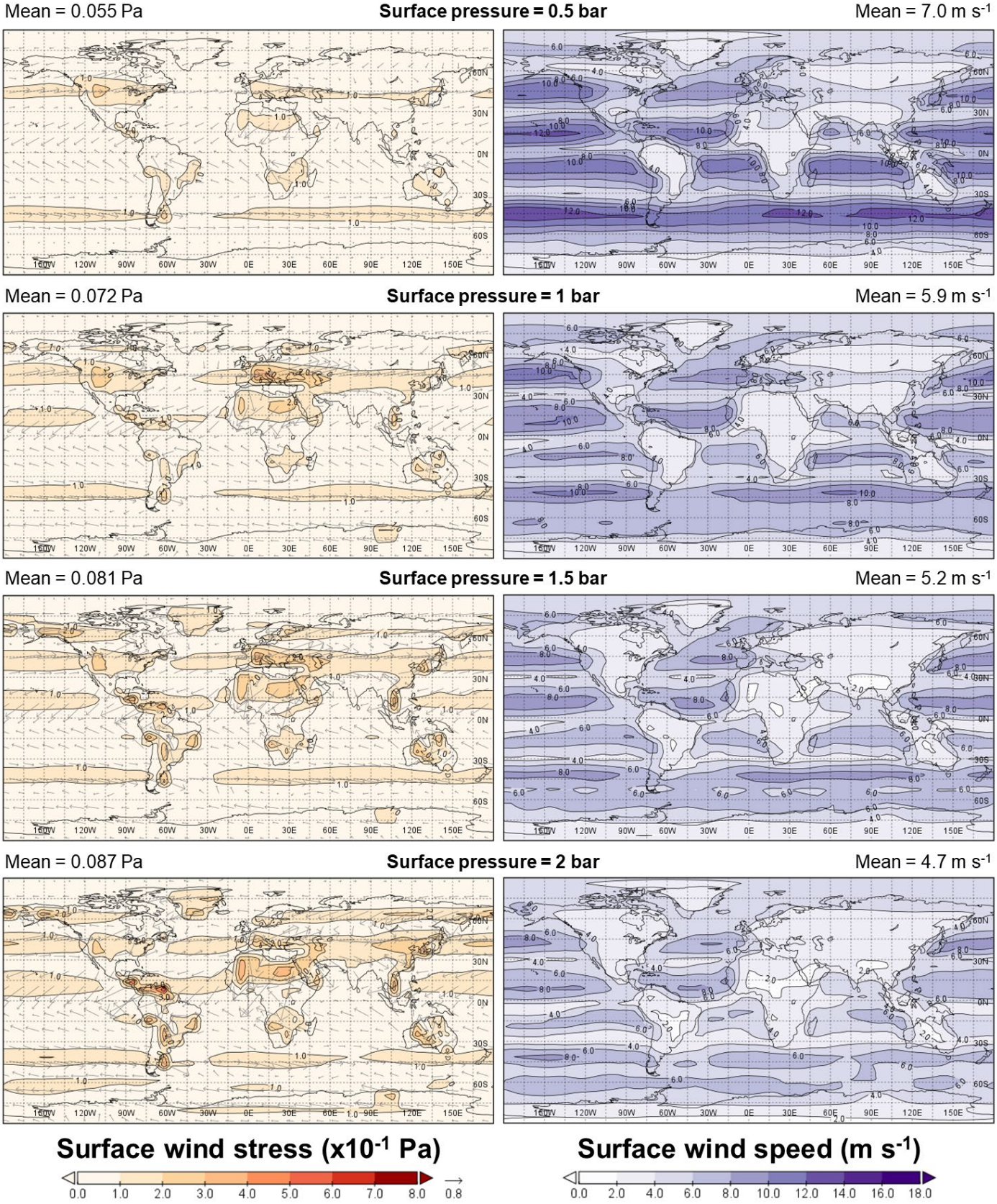

Figure S-13 Annual mean surface wind stress and speed in ozone-less baseline *vs*. surface pressure sensitivity tests.

Supplementary Information References

Table S-1 compiles the parameter values used in the modelling the Nd cycle during the Archean.

	Scenario 1	Scenario 2	Scenario 3		Scenario 4	
Seawater [Nd] (g/kg)	1.43×10^{-7}	3.37×10^{-8}	Same as Scenario 1		Same as Scenario 2	
Seawater ε_{Nd}	+0.63	Same as Scenario 1			Same as Scenario 1	
Hydrothermal Nd source (g/yr)	1.25×10^{10}					
Hydrothermal flux ε_{Nd}	+2.6					
Riverine Nd source (g/yr)	2.76×10^{9}				1.35×10^{9}	1.41×10^{9}
Riverine flux ε_{Nd}	-0.42				-3.1	+3.4
Dust Nd source (g/yr)	2.86×10^{8}				1.40×10^{8}	1.46×10^{8}
Dust flux ε_{Nd}	-0.42				-3.1	+3.4
Sediment Nd source (g/yr)	2.95×10^{11}	5.79×10^{10}	2.00×10^{11}	9.50×10^{10}	2.83×10^{10}	2.96×10^{10}
Sediment flux ε_{Nd}	+0.56	+0.26	-0.42	+2.6	-3.1	+3.4

Supplementary Information References

Abbott, A.N., Haley, B.A., McManus, J. (2015a) Bottoms up: Sedimentary control of the deep North Pacific Ocean's εNd signature. *Geology* 43, 1035-1035. https://doi.org/10.1130/G37114.1

Abbott, A.N., Haley, B.A., McManus, J., Reimers, C.E. (2015b) The sedimentary flux of dissolved rare earth elements to the ocean. *Geochimica et Cosmochimica Acta* 154, 186-200. https://doi.org/10.1016/j.gca.2015.01.010

Alexander, B.W., Bau, M., Andersson, P., Dulski, P. (2008) Continentally-derived solutes in shallow Archean seawater: rare earth element and Nd isotope evidence in iron formation from the 2.9 Ga Pongola Supergroup, South Africa. *Geochimica et Cosmochimica Acta* 72, 378-394. https://doi.org/10.1016/j.gca.2007.10.028

Alibert, C., McCulloch, M.T. (1993) Rare earth element and neodymium isotopic compositions of the banded iron-formations and associated shales from Hamersley, Western Australia. *Geochimica et Cosmochimica Acta* 57, 187-204. https://doi.org/10.1016/0016-7037(93)90478-F

Bacon, M.P., Anderson, R.F. (1982) Distribution of thorium isotopes between dissolved and particulate forms in the deep sea. *Journal of Geophysical Research: Oceans* 87, 2045-2056. https://doi.org/10.1029/JC087iC03p02045

Crichton, K.A., Ridgwell, A., Lunt, D.J., Farnsworth, A., Pearson, P.N. (2021) Data-constrained assessment of ocean circulation changes since the middle Miocene in an Earth system model. *Climate of the Past* 17, 2223-2254. https://doi.org/10.5194/cp-17-2223-2021

Dauphas, N., Heard, A.W., Rego, E.S., Rouxel, O., Marin-Carbonne, J., Pasquier, V., Bekker, A., Rowley, D.B., (2024) Past and present dynamics of the iron biogeochemical cycle. *Reference Module in Earth Systems and Environmental Sciences*. https://doi.org/10.1016/B978-0-323-99762-1.00059-0

Davies, H.S., Green, J.A.M., Duarte, J.C. (2020) Back to the future II: tidal evolution of four supercontinent scenarios. *Earth System Dynamics* 11, 291–299. https://doi.org/10.5194/esd-11-291-2020

Du, J., Haley, B.A., Mix, A.C., Walczak, M.H., Praetorius, S.K. (2018) Flushing of the deep Pacific Ocean and the deglacial rise of atmospheric CO2 concentrations. *Nature Geoscience* 11, 749-755. https://doi.org/10.1038/s41561-018-0205-6

Du, J., Haley, B.A., Mix, A.C. (2020) Evolution of the Global Overturning Circulation since the Last Glacial Maximum based on marine authigenic neodymium isotopes. *Quaternary Science Reviews* 241, 106396. https://doi.org/10.1016/j.quascirev.2020.106396

Fraedrich, K., Jansen, H., Kirk, E., Luksch, U., Lunkeit, F. (2005) The Planet Simulator: Towards a user friendly model. *Meteorologische Zeitschrift* 14, 299-304. https://doi.org/10.1127/0941-2948/2005/0043

Frei, R., Dahl, P.S., Duke, E.F., Frei, K.M., Hansen, T.R., Frandsson, M.M., Jensen, L.A. (2008) Trace element and isotopic characterization of Neoarchean and Paleoproterozoic iron formations in the Black Hills (South Dakota, USA): assessment of chemical change during 2.9–1.9 Ga deposition bracketing the 2.4–2.2 Ga first rise of atmospheric oxygen. *Precambrian Research* 162, 441-474. https://doi.org/10.1016/j.precamres.2007.10.005

Garçon, M. (2021) Episodic growth of felsic continents in the past 3.7 Ga. *Science advances* 7, eabj1807. DOI: 10.1126/sciadv.abj1807

German, C.R., Klinkhammer, G.P., Edmond, J.M., Mura, A., Elderfield, H. (1990) Hydrothermal scavenging of rare-earth elements in the ocean. *Nature* 345, 516-518. https://doi.org/10.1038/345516a0

Ghosh, R., Baidya, T.K. (2017) Using BIF magnetite of the Badampahar greenstone belt, Iron Ore Group, East Indian Shield to reconstruct the water chemistry of a 3.3–3.1 Ga sea during iron oxyhydroxides precipitation. *Precambrian Research* 301, 102-112. https://doi.org/10.1016/j.precamres.2017.09.006

Goldstein, S.J., Jacobsen, S.B. (1987) The Nd and Sr isotopic systematics of river-water dissolved material: Implications for the sources of Nd and Sr in seawater. *Chemical Geology: Isotope Geoscience section* 66, 245-272. https://doi.org/10.1016/0168-9622(87)90045-5

Goldstein, S.L., O'nions, R.K., Hamilton, P.J. (1984) A Sm-Nd isotopic study of atmospheric dusts and particulates from major river systems. *Earth and Planetary Science letters* 70, 221-236. https://doi.org/10.1016/0012-821X(84)90007-4

Greaves, M.J., Statham, P.J., Elderfield, H. (1994) Rare earth element mobilization from marine atmospheric dust into seawater. *Marine Chemistry* 46, 255-260. https://doi.org/10.1016/0304-4203(94)90081-7

Haley, B.A., Du, J., Abbott, A.N., McManus, J. (2017) The impact of benthic processes on rare earth element and neodymium isotope distributions in the oceans. *Frontiers in Marine Science* 4, 426. https://doi.org/10.3389/fmars.2017.00426

Haugaard, R., Ootes, L., Creaser, R.A., Konhauser, K.O. (2016) The nature of Mesoarchaean seawater and continental weathering in 2.85 Ga banded iron formation, Slave craton, NW Canada. *Geochimica et Cosmochimica Acta* 194, 34-56. https://doi.org/10.1016/j.gca.2016.08.020

Jacobsen, S.B., Pimentel-Klose, M.R. (1988) A Nd isotopic study of the Hamersley and Michipicoten banded iron formations: the source of REE and Fe in Archean oceans. *Earth and Planetary Science Letters* 87, 29-44. https://doi.org/10.1016/0012-821X(88)90062-3

Korenaga, J. (2008) Urey ratio and the structure and evolution of Earth's mantle. *Reviews of Geophysics* 46, RG2007. https://doi.org/10.1029/2007RG000241

Korenaga, J., Planavsky, N.J., Evans, D.A. (2017) Global water cycle and the coevolution of the Earth's interior and surface environment. *Philosophical Transactions of the Royal Society A: Mathematical, Physical and Engineering Sciences* 375, 20150393. https://doi.org/10.1098/rsta.2015.0393

Krissansen-Totton, J., Arney, G.N., Catling, D.C. (2018) Constraining the climate and ocean pH of the early Earth with a geological carbon cycle model. *Proceedings of the National Academy of Sciences* 115, 4105-4110. https://doi.org/10.1073/pnas.1721296115

Kunze, E., Firing, E., Hummon, J.M., Chereskin, T.K., Thurnherr, A.M. (2006) Global Abyssal Mixing Inferred from Lowered ADCP Shear and CTD Strain Profiles. *Journal of Physical Oceanography* 36, 1553–1576. https://doi.org/10.1175/JPO2926.1

Lowell, R.P., Keller, S.M. (2003) High-temperature seafloor hydrothermal circulation over geologic time and Archean banded iron formations. *Geophysical Research Letters* 30, 1391. https://doi.org/10.1029/2002GL016536

Oliver, K.I.C., Edwards, N.R. (2008) Location of potential energy sources and the export of dense water from the Atlantic Ocean. *Geophysical Research Letters* 35, L22604. https://doi.org/10.1029/2008GL035537

Paradise, A., Fan, B.L., Menou, K., Lee, C. (2021) Climate diversity in the solar-like habitable zone due to varying background gas pressure. *Icarus* 358, 114301. https://doi.org/10.1016/j.icarus.2020.114301

Paradise, A., Macdonald, E., Menou, K., Lee, C., Fan, B.L. (2022) ExoPlaSim: Extending the Planet Simulator for exoplanets. *Monthly Notices of the Royal Astronomical Society* 511, 3272-3303. https://doi.org/10.1093/mnras/stac172

Patočka, V., Šrámek, O., Tosi, N. (2020) Minimum heat flow from the core and thermal evolution of the Earth. *Physics of the Earth and Planetary Interiors* 305, 106457. https://doi.org/10.1016/j.pepi.2020.106457

Ptáček, M.P., Dauphas, N., Greber, N.D. (2020) Chemical evolution of the continental crust from a data-driven inversion of terrigenous sediment compositions. *Earth and Planetary Science Letters* 539, 116090. https://doi.org/10.1016/j.epsl.2020.116090

Rempfer, J., Stocker, T.F., Joos, F., Dutay, J.C., Siddall, M. (2011) Modelling Nd-isotopes with a coarse resolution ocean circulation model: Sensitivities to model parameters and source/sink distributions. *Geochimica et Cosmochimica Acta* 75, 5927-5950. https://doi.org/10.1016/j.gca.2011.07.044

Ridgwell, A. (2017) The Bumper Book of muffins (The cGENIE.muffin user-manual and introduction to Earth system modelling). https://www.seao2.info/cgenie/docs/muffin.pdf

Robinson, S., Ivanovic, R.F., Gregoire, L.J., Tindall, J., van de Flierdt, T., *et al.* (2023) Simulating marine neodymium isotope distributions using Nd v1. 0 coupled to the ocean component of the FAMOUS–MOSES1 climate model: sensitivities to reversible scavenging efficiency and benthic source distributions. *Geoscientific Model Development* 16, 1231-1264. https://doi.org/10.5194/gmd-16-1231-2023

Trendall, A.F. (2002) The significance of iron-formation in the Precambrian stratigraphic record. *Precambrian sedimentary environments: A modern approach to ancient depositional systems*, 33-66. https://doi.org/10.1002/9781444304312.ch3

Vervoort, J.D., Blichert-Toft, J. (1999) Evolution of the depleted mantle: Hf isotope evidence from juvenile rocks through time. *Geochimica et Cosmochimica Acta* 63, 533-556. https://doi.org/10.1016/S0016-7037(98)00274-9

Waterhouse, A.F., Mackinnon, J.A., Nash, J.D., Alford, M.H., Kunze, E., *et al.* (2014) Global Patterns of Diapycnal Mixing from Measurements of the Turbulent Dissipation Rate. *Journal of Physical Oceanography* 44, 1854–1872. https://doi.org/10.1175/JPO-D-13-0104.1

Webb, D.J. (1982) Tides and the evolution of the Earth-Moon system. *Geophysical Journal International* 70, 261–271. https://academic.oup.com/gji/article-abstract/70/1/261/708791

Wu, C., Lin, Z., Liu, X. (2020) The global dust cycle and uncertainty in CMIP5 (Coupled Model Intercomparison Project phase 5) models. *Atmospheric Chemistry and Physics* 20, 10401-10425. https://doi.org/10.5194/acp-20-10401-2020

Xu, A., Hathorne, E., Laukert, G., Frank, M. (2023) Overlooked riverine contributions of dissolved neodymium and hafnium to the Amazon estuary and oceans. *Nature Communications* 14, 4156. https://doi.org/10.1038/s41467-023-39922-3

Yamamoto, K., Itoh, N., Matsumoto, T., Tanaka, T., Adachi, M. (2004) Geochemistry of Precambrian carbonate intercalated in pillows and its host basalt: implications for the REE composition of circa 3.4 Ga seawater. *Precambrian Research* 135, 331-344. https://doi.org/10.1016/j.precamres.2004.09.006

Yang, J., Jansen, M.F., Macdonald, F.A., Abbot, D.S. (2017) Persistence of a freshwater surface ocean after a snowball Earth. *Geology* 45, 615–618. https://doi.org/10.1130/G38920.1